EXPONENTIAL FINITE ELEMENT SHAPE FUNCTIONS FOR A PHASE FIELD MODEL OF BRITTLE FRACTURE

CHARLOTTE KUHN[*] AND RALF MÜLLER[†]

Institute of Applied Mechanics
Technische Universität Kaiserslautern
P.O.B. 3049, 67653 Kaiserslautern
http://mechanik.mv.uni-kl.de/
[*]e-mail: chakuhn@rhrk.uni-kl.de

[†]e-mail: ram@rhrk.uni-kl.de

Key words: Phase Field Model, Fracture, Finite Elements, Exponential Shape Functions

Abstract. In phase field models for fracture a continuous scalar field variable is used to indicate cracks, i.e. the value 1 of the phase field variable is assigned to sound material, while the value 0 indicates fully broken material. The width of the transition zone where the phase field parameter changes between 1 and 0 is controlled by a regularization parameter. As a finite element discretization of the model needs to be fine enough to resolve the crack field and its gradient, the numerical results are sensitive to the choice of the regularization parameter in conjunction with the mesh size. This is the main challenge and the computational limit of the finite element implementation of phase field fracture models. To overcome this limitation a finite element technique using special shape functions is introduced. These special shape functions take into account the exponential character of the crack field as well as its dependence on the regularization length. Numerical examples show that the exponential shape functions allow a coarser discretization than standard linear shape functions without compromise on the accuracy of the results. This is due to the fact, that using exponential shape functions, the approximation of the surface energy of the phase field cracks is impressively precise, even if the regularization length is rather small compared to the mesh size. Thus, these shape functions provide an alternative to a numerically expensive mesh refinement.

1 INTRODUCTION

Variational formulations of brittle fracture as suggested by Francfort and Marigo [1] overcome some of the limitations of classical Griffith theory. However, a direct discretization of such fracture models is faced with significant technical difficulties. A regularized approximation by means of Γ-convergence as presented by Bourdin [2] offers a new

perspective towards the computational implementation of the model. The core of the regularization is the approximation of the total energy functional, in which a continuous scalar field variable is introduced to indicate cracks, i.e. the value of 1 is assigned to sound material and a value of 0 indicates fracture. With this crack field the regularized model resembles a phase field model for fracture, where additionally a Ginzburg–Landau type equation is used to describe the evolution of the crack field and cracking is addressed as a phase transition problem. Similar phase field fracture models have been introduced e.g. in [3, 4, 5, 6, 7, 8]. Differing in technical details all of these models introduce a regularization length which controls the width of the transition zone where the crack field interpolates between broken and unbroken material; i.e. the smaller the regularization parameter, the smaller the transition zone and the higher the gradients of the crack field in the vicinity of the cracks.

Numerical implementations are faced with the difficulty that the spacial discretization has to be fine enough to resolve these high gradients of the crack field, which leads to high computational costs for small values of the regularization parameter. On the other hand the regularization length needs to be chosen sufficiently small in conjunction with the global geometric dimension of the sample in order to get reasonable results. The most common approach to meet the requirement for a sufficiently fine resolution on the one hand and to keep the computation time within bounds on the other hand are adaptive mesh refinement techniques as used e.g. in [9], where the mesh is only refined where it is necessary, i.e. in the vicinity of a crack. Another approach to increase the efficiency of the computations was introduced in [5], where Fourier transforms are used to solve the linear part of the problem. However, this technique restricts the simulations to problems with periodic boundary conditions.

In this work we follow a different approach which is inspired by [10], where exponential finite element (FE) shape functions are introduced as an alternative to an extensive mesh refinement in the simulation of extrusion processes. These special shape functions qualitatively capture the shape of the solution and thus allow a much coarser discretization than the standard discretization using linear shape functions. In contrast to the simulation of the extrusion process, where the exponential shape functions are used in one distinct direction only, the discretization of the crack field in a two dimensional setting requires an extension of the concept to the full 2d case.

2 A PHASE FIELD MODEL FOR FRACTURE

2.1 Governing Equations

The present phase field model of fracture is based on a regularized version of the variational formulation of brittle fracture by [1] which was introduced in [11]. The core of the regularization is the approximation of the total energy of a cracked linear elastic

body Ω, with the stiffness tensor $\mathbb{C}$ and the cracking resistance $\mathcal{G}_c$, by the functional

$$E(\boldsymbol{\varepsilon}, s) = \int_\Omega \psi(\boldsymbol{\varepsilon}, s) \, dV = \int_\Omega \underbrace{\frac{1}{2}(s^2 + \eta)\boldsymbol{\varepsilon} \cdot (\mathbb{C}\boldsymbol{\varepsilon})}_{=\psi^{\mathrm{e}}(\boldsymbol{\varepsilon}, s)} + \underbrace{\mathcal{G}_c \left(\frac{1}{4\epsilon}(1-s)^2 + \epsilon|\nabla s|^2 \right)}_{=\psi^{\mathrm{s}}(s)} dV \,. \quad (1)$$

This energy as well as the energy density ψ are functions of the linearized strain tensor $\boldsymbol{\varepsilon} = \frac{1}{2}(\nabla\boldsymbol{u} + (\nabla\boldsymbol{u})^T)$, i.e. the symmetric part of the gradient of the displacements $\boldsymbol{u}$ and the continuous scalar crack field s, which takes the value 1, if the material is undamaged, and 0 if there is a crack. The degradation of the elastic energy in the bulk $E^{\mathrm{e}} = \int_\Omega \psi^{\mathrm{e}} \, dV$ upon cracking is modeled by the factor $(s^2 + \eta)$, where the small positive parameter η is introduced to obtain an artificial rest stiffness $\eta\mathbb{C}$ at fully broken state $(s = 0)$ in order to circumvent numerical difficulties. The parameter ϵ, appearing twice in the surface energy $E^{\mathrm{s}} = \int_\Omega \psi^{\mathrm{s}} \, dV$, has the dimension of length and controls the width of the transition zone between broken and unbroken material, where s interpolates between 0 and 1.

If body forces and inertia terms are neglected, the mechanical part of the problem is described by the local balance law for the Cauchy stress tensor $\boldsymbol{\sigma}$

$$\mathrm{div}\boldsymbol{\sigma} = \boldsymbol{0} \,, \quad (2)$$

plus the according boundary conditions $\boldsymbol{\sigma}\boldsymbol{n} = \boldsymbol{t}_n^*$ on $\partial\Omega_t$, where $\boldsymbol{n}$ is the outer normal vector, and the material law (3) derived from the energy density ψ

$$\boldsymbol{\sigma} = \frac{\partial\psi}{\partial\boldsymbol{\varepsilon}} = (s^2 + \eta)\mathbb{C}\boldsymbol{\varepsilon} \,. \quad (3)$$

Interpreting s as order parameter of a phase field model, its evolution in time is assumed to follow a Ginzburg–Landau type evolution equation, where $\dot{s}$ is proportional to the variational derivative of the energy density ψ with respect to s.

$$\dot{s} = -M \cdot \frac{\delta\psi}{\delta s} = -M \left[s\boldsymbol{\varepsilon} \cdot (\mathbb{C}\boldsymbol{\varepsilon}) - \mathcal{G}_c \left(2\epsilon\Delta s + \frac{1-s}{2\epsilon} \right) \right] \quad (4)$$

The mobility factor M is a positive constant, which controls the dissipation in the process zone. For sufficiently large values of M the solution of the evolution equation can be considered as stationary. In order to take into consideration the irreversible character of cracking, $s(\boldsymbol{x}, t)$ is fixed to 0 for all future times $t > t^*$ if it becomes 0 at any time t^*.

2.2 Evolution Equation in 1d

In a 1d setting, the evolution equation for a stationary $(\dot{s} = 0)$ crack field reduces to

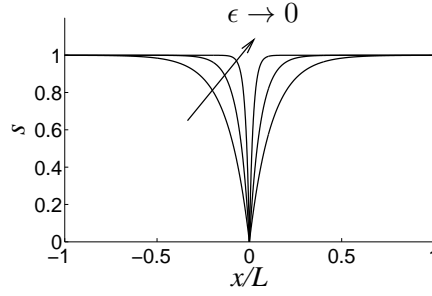$$s'' - \frac{s}{4\epsilon^2} = -\frac{1}{4\epsilon^2} \,, \quad (5)$$

Figure 1: 1d stationary crack field

if elastic contributions are neglected. With boundary conditions $s(0) = 0$ and $s'(\pm\infty) = 0$ the analytic solution of Eq. (5) is given by

$$s(x) = 1 - \exp\left(-\frac{|x|}{2\epsilon}\right) \tag{6}$$

Figure 1 illustrates the impact of the regularization length ϵ on the crack field $s(x)$. The smaller ϵ gets, the higher gradients and curvatures of the solution $s(x)$ appear in the vicinity of the crack at $x = 0$. The limit $\epsilon \to 0$ yields a discontinuous function, which is 0 at $x = 0$ and 1 elsewhere.

3 NUMERICAL IMPLEMENTATION

3.1 Weak Forms

Starting point for the FE implementation of the coupled problem of mechanical balance equation (2) and evolution equation (4) are the weak forms of these field equations. With virtual displacements $\delta\boldsymbol{u}$ and δs, they read

$$\int_{\Omega} \nabla\delta\boldsymbol{u} \cdot \boldsymbol{\sigma}\, dV = \int_{\partial\Omega_t} \delta\boldsymbol{u} \cdot \boldsymbol{t}_n^*\, dA \tag{7}$$

with prescribed surface traction $\boldsymbol{t}_n^*$ on part $\partial\Omega_t$ of the boundary and

$$\int_{\Omega} \left[\delta s\frac{\dot{s}}{M} - \nabla\delta s \cdot \boldsymbol{q} + \delta s\left(s\boldsymbol{\varepsilon} : [\mathbb{C}\boldsymbol{\varepsilon}] + \frac{\mathcal{G}_c}{2\epsilon}(s-1)\right)\right] dV = 0 \tag{8}$$

with $\boldsymbol{q} = -2\mathcal{G}_c\,\epsilon\,\nabla s$. The normal flux $\boldsymbol{q} \cdot \boldsymbol{n}$ is assumed to vanish on the boundary $\partial\Omega$.

3.2 Finite Element Discretization

In a 2d setting the weak forms of the field equations (7) and (8) are discretized with 4 node quadrilateral elements with 3 degrees of freedom (u_x, u_y, s) per node. The displacements $\boldsymbol{u}$, the crack field s, as well as their virtual counterparts $\delta\boldsymbol{u}$ and δs are approximated

by shape functions $N_I^{\boldsymbol{u}}$, N_I^s, $N_I^{\delta\boldsymbol{u}}$, and $N_I^{\delta s}$, which interpolate the respective nodal values $\hat{\boldsymbol{u}}_I$, $\hat{s}_I$, $\delta\hat{\boldsymbol{u}}_I$, and $\delta\hat{s}_I$. Using Voigt–notation - denoted by an underline in the following - the approximations read

$$\underline{\boldsymbol{u}} = \sum_{I=1}^N N_I^{\boldsymbol{u}}\underline{\hat{\boldsymbol{u}}}_I\,,\quad s = \sum_{I=1}^N N_I^s\hat{s}_I\,,\quad \underline{\delta\boldsymbol{u}} = \sum_{I=1}^N N_I^{\delta\boldsymbol{u}}\underline{\delta\hat{\boldsymbol{u}}}_I\,,\quad \text{and}\quad \delta s = \sum_{I=1}^N N_I^{\delta s}\delta\hat{s}_I\,. \quad (9)$$

Accordingly the approximations of the gradient expressions yield

$$\underline{\boldsymbol{\varepsilon}} = \sum_{I=1}^N [\underline{B}_I^{\boldsymbol{u}}]\underline{\hat{\boldsymbol{u}}}_I,\quad \underline{\nabla s} = \sum_{I=1}^N [\underline{B}_I^s]\hat{s}_I,\quad \underline{\delta\boldsymbol{\varepsilon}} = \sum_{I=1}^N [\underline{B}_I^{\delta\boldsymbol{u}}]\underline{\delta\hat{\boldsymbol{u}}}_I,\quad \text{and}\ \underline{\nabla\delta s} = \sum_{I=1}^N [\underline{B}_I^{\delta s}]\delta\hat{s}_I\,, \quad (10)$$

where the derivative matrices

$$[\underline{B}_I^{\boldsymbol{u}}] = \begin{bmatrix} N_{I,x}^{\boldsymbol{u}} & 0 \\ 0 & N_{I,y}^{\boldsymbol{u}} \\ N_{I,y}^{\boldsymbol{u}} & N_{I,x}^{\boldsymbol{u}} \end{bmatrix}\,,\ [\underline{B}_I^s] = \begin{bmatrix} N_{I,x}^s \\ N_{I,y}^s \end{bmatrix}\,,\ [\underline{B}_I^{\delta\boldsymbol{u}}] = \begin{bmatrix} N_{I,x}^{\delta\boldsymbol{u}} & 0 \\ 0 & N_{I,y}^{\delta\boldsymbol{u}} \\ N_{I,y}^{\delta\boldsymbol{u}} & N_{I,x}^{\delta\boldsymbol{u}} \end{bmatrix}\,,\ \text{and}\ [\underline{B}_I^{\delta s}] = \begin{bmatrix} N_{I,x}^{\delta s} \\ N_{I,y}^{\delta s} \end{bmatrix} \quad (11)$$

are obtained from the derivatives of the shape functions.

By a standard argument for finite element approximations the nodal values $\delta\hat{\boldsymbol{u}}_I$ and $\delta\hat{s}_I$ of the virtual quantities $\delta\boldsymbol{u}$ and δs drop out of the system of equations, leading to the nodal residuals

$$[\underline{R}_I] = \begin{bmatrix} \underline{R}_I^{\boldsymbol{u}} \\ R_I^s \end{bmatrix} = \int_\Omega \begin{bmatrix} [\underline{B}_I^{\delta\boldsymbol{u}}]^T\underline{\boldsymbol{\sigma}} \\ N_I^{\delta s}\dfrac{\dot{s}}{M} - [\underline{B}_I^{\delta s}]^T\underline{\boldsymbol{q}} + N_I^{\delta s}\left(s\,\underline{\boldsymbol{\varepsilon}}^T\cdot(\mathbb{C}\,\underline{\boldsymbol{\varepsilon}}) + \dfrac{\mathcal{G}_c}{2\,\epsilon}(s-1)\right) \end{bmatrix}dV\,. \quad (12)$$

The time integration of the transient terms is performed with the implicit Euler method. Together with the nonlinear character of the phase field model this yields a nonlinear system of equations, which has to be solved in every time step Δt. This is done with a Newton–Raphson algorithm, which requires the derivation of the consistent tangent matrix $[\underline{S}_{IJ}]$ which has the following structure:

$$[\underline{S}_{IJ}] = [\underline{K}_{IJ}] + \frac{1}{\Delta t}[\underline{D}_{IJ}]\,. \quad (13)$$

The stiffness matrix $[\underline{K}_{IJ}]$ and the damping matrix $[\underline{D}_{IJ}]$ are obtained by derivation of the nodal residuals $[\underline{R}_I]$ with respect to the nodal values $(\hat{\underline{\boldsymbol{u}}}_J, \hat{s}_J)$ and $(\dot{\hat{\underline{\boldsymbol{u}}}}_J, \dot{\hat{s}}_J)$, respectively.

$$[\underline{K}_{IJ}] = \int_\Omega \begin{bmatrix} [\underline{B}_I^{\delta\boldsymbol{u}}]^T(s^2+\eta)\,\mathbb{C}\,[\underline{B}_J^{\boldsymbol{u}}] & [\underline{B}_I^{\delta\boldsymbol{u}}]^T 2s\,\mathbb{C}\,\underline{\boldsymbol{\varepsilon}}N_J^s \\ N_I^{\delta s}2s(\mathbb{C}\,\underline{\boldsymbol{\varepsilon}})^T[\underline{B}_J^{\boldsymbol{u}}] & 2\mathcal{G}_c\,\epsilon\,[\underline{B}_I^{\delta s}]^T[\underline{B}_J^s] + N_I^{\delta s}\left(\underline{\boldsymbol{\varepsilon}}^T\cdot\mathbb{C}\,\underline{\boldsymbol{\varepsilon}} + \dfrac{\mathcal{G}_c}{2\,\epsilon}\right)N_J^s \end{bmatrix}dV \quad (14)$$
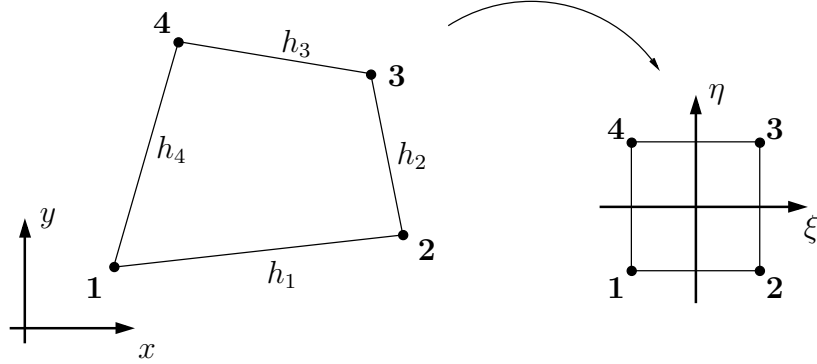
Figure 2: Node and edge numbering of the quadrilateral element in global (left) and natural coordinates (right)

and

$$\left[\underline{D}_{IJ}\right] = \int_\Omega \begin{bmatrix} 0 & 0 \\ 0 & \dfrac{1}{M}N_I^{\delta s}N_J^s \end{bmatrix} dV \,. \tag{15}$$

If the same shape functions are chosen for the approximation of actual values and the virtual quantities, i.e. $N_I^{\boldsymbol{u}} = N_I^{\delta \boldsymbol{u}}$ and $N_I^s = N_I^{\delta s}$, the system matrix $\left[\underline{S}_{IJ}\right]$ becomes symmetric. This is due to the fact, that the constitutive law (3) as well as the evolution equation (4) are derived from a potential. Different shape functions however, render a non-symmetric system matrix $\left[\underline{S}_{IJ}\right]$.

4 EXPONENTIAL SHAPE FUNCTIONS

The standard implementation with 4 node quadrilateral elements makes use of the linear Lagrangian shape functions

$$N_I^{\text{lin}}(\xi,\eta) = \frac{1}{4}(1 + \xi_I\xi)(1 + \eta_I\eta), \qquad I = 1,...,4 \tag{16}$$

with (ξ_I, η_I) according to Fig. 2 for all the shape functions $N_I^{\boldsymbol{u}}$, $N_I^{\delta \boldsymbol{u}}$, N_I^s, and $N_I^{\delta s}$ as well as for the approximation of the geometry in the isoparametric concept

$$\boldsymbol{x} = \sum_{I=1}^N N_I^{\text{lin}}\hat{\boldsymbol{x}}_I. \tag{17}$$

In [12] it is shown that triangular elements with linear shape functions overestimate the surface energy by a factor

$$f(h/\epsilon) = 1 + h/4\epsilon\,, \tag{18}$$

where h is the edge length of the elements. As a sufficiently good approximation of the surface energy is crucial in order to obtain reasonable results, this yields the necessity of a
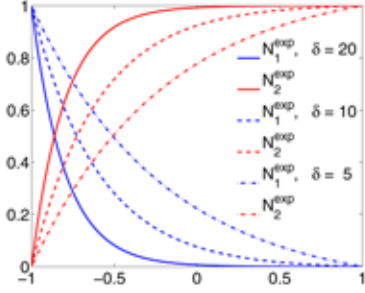
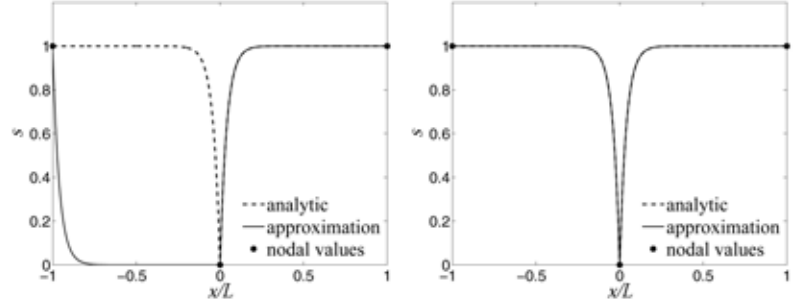Figure 3: 1d exponential shape functions for different values of δ

Figure 4: Approximation with unswitched shape functions (left), and switched shape functions (right)

very fine resolution of the transition zones. In different numerical simulations with linear shape functions in a 2d setting, $h \approx \epsilon$ was empirically found as an upper bound for the element size, [13, 8].

4.1 1d Exponential Shape Functions

The simulation of extrusion processes is faced with a similar problem, as shear boundary layers which exhibit an exponential velocity profile need to be resolved. In [10] exponential shape functions, that qualitatively capture the shape of the sharp velocity field, are proposed as an alternative to a fine spacial resolution. Adapted to the present phase field model these 1d shape functions read

$$\bar{N}_1^{\exp}(\xi, \delta) = 1 - \frac{\exp\left(-\frac{\delta(1+\xi)}{4}\right) - 1}{\exp\left(-\frac{\delta}{2}\right) - 1} \quad \text{and} \tag{19}$$

$$\bar{N}_2^{\exp}(\xi, \delta) = \frac{\exp\left(-\frac{\delta(1+\xi)}{4}\right) - 1}{\exp\left(-\frac{\delta}{2}\right) - 1} \tag{20}$$

in natural coordinates on the interval $[-1, 1]$. Through their dependence on the ratio $\delta = h/\epsilon$ of the element size h and the regularization parameter ϵ, these shape functions are able to capture the analytic solution (6) for any values of h and ε. In the limit case $\delta \to 0$ or equivalently $h \to 0$ these shape functions converge to the one dimensional linear shape functions, see also Fig. 3.

$$\lim_{\delta \to 0} \bar{N}_1^{\exp}(\xi, \delta) = \frac{1-\xi}{2} = N_1^{\lin}(\xi) \qquad \lim_{\delta \to 0} \bar{N}_2^{\exp}(\xi, \delta) = \frac{1+\xi}{2} = N_2^{\lin}(\xi) \tag{21}$$

The exponential shape functions (19) and (20) are unsymmetric with respect to ξ, i.e. $\bar{N}_1^{\exp}(-\xi) \neq \bar{N}_2^{\exp}(\xi)$, and are designed to match the analytical solution (6), if $\hat{s}_1 \leq \hat{s}_2$ (presuming node numbering from left to right) holds for the according nodal values, see Fig. 4. Due to their non-symmetry the shape functions need to be switched according to

the nodal values of s in order to obtain good approximations for arbitrary nodal values of s.

$$N_1^{\text{exp}}(\xi) = \begin{cases} \bar{N}_1^{\text{exp}}(\xi, \delta) & \text{if } \hat{s}_1 \leq \hat{s}_2 \\ \bar{N}_2^{\text{exp}}(-\xi, \delta) & \text{if } \hat{s}_1 > \hat{s}_2 \end{cases} \quad \text{and} \quad N_2^{\text{exp}}(\xi) = \begin{cases} \bar{N}_2^{\text{exp}}(\xi, \delta) & \text{if } \hat{s}_1 \leq \hat{s}_2 \\ \bar{N}_1^{\text{exp}}(-\xi, \delta) & \text{if } \hat{s}_1 > \hat{s}_2 \end{cases} \quad (22)$$

4.2 Extension to the 2d Setting

The 2d linear shape function (16) of each single element node can be obtained by multiplying the 1d linear shape functions belonging to the adjacent edges of the respective node. Replacing the 1d linear shape functions by the exponential shape functions (22) this strategy yields

$$\begin{array}{ll} N_1^{\text{exp}}(\xi, \eta, \delta_i) = N_1^{\text{exp}}(\xi, \delta_1) \cdot N_1^{\text{exp}}(\eta, \delta_4), & N_2^{\text{exp}}(\xi, \eta, \delta_i) = N_2^{\text{exp}}(\xi, \delta_1) \cdot N_1^{\text{exp}}(\eta, \delta_2), \\ N_3^{\text{exp}}(\xi, \eta, \delta_i) = N_2^{\text{exp}}(\xi, \delta_3) \cdot N_2^{\text{exp}}(\eta, \delta_2), & N_4^{\text{exp}}(\xi, \eta, \delta_i) = N_1^{\text{exp}}(\xi, \delta_3) \cdot N_2^{\text{exp}}(\eta, \delta_4), \end{array} \quad (23)$$

where the element nodes and the element edges are numbered according to Fig. 2. Each shape function depends on the ratio $\delta_i = \frac{h_i}{\epsilon}$ of both adjacent element edges. For an appropriate approximation behavior, it is postulated that the orientation of the 1d shape functions of opposite edges must be the same. The so constructed shape functions possess the Kronecker delta property, i.e. $N_I^{\text{exp}}(\xi_J, \eta_J, \delta_i) = \delta_{IJ}$. Continuity across element borders holds, if the orientation of the shared edge of two neighbor elements is the same. However, the partition of unity property does not hold in general, i.e. it holds only if

$$\delta_1 = \delta_3 \qquad \text{or} \qquad \delta_2 = \delta_4 \,. \tag{24}$$

For the sake of simplicity, we restrict the element shape at this point to square and rectangular elements for which condition (24) holds. For a more general framework allowing for arbitrarily shaped quadrilateral elements, as well as for some more technical details of the implementation, the reader is referred to [14].

5 NUMERICAL EXAMPLES

The performance of the exponential shape functions is tested in this section. In all simulations, linear shape functions (16) were used for the approximation of the geometry and the actual and virtual displacements, i.e. $N_I^{\boldsymbol{u}} = N_I^{\delta\boldsymbol{u}} = N_I^{\text{lin}}$. Three different versions of approximating the crack field s and its virtual counterpart δs are compared to each other: The standard approximation with linear shape functions $N_I^s = N_I^{\delta s} = N_I^{\text{lin}}$ (labeled lin/lin), the complete approximation with exponential shape functions $N_I^s = N_I^{\delta s} = N_I^{\text{exp}}$ (labeled exp/exp), and a mixed formulation with $N_I^s = N_I^{\text{exp}}$ but $N_I^{\delta s} = N_I^{\text{lin}}$ (labeled lin/exp).

5.1 Evolution Equation in 1d

As a first test, the 1d stationary evolution equation (5) is solved for a regularization parameter $\epsilon = 0.01L$. The superior performance of the exponential shape functions becomes apparent in the plots of the numerical solutions with different numbers of elements
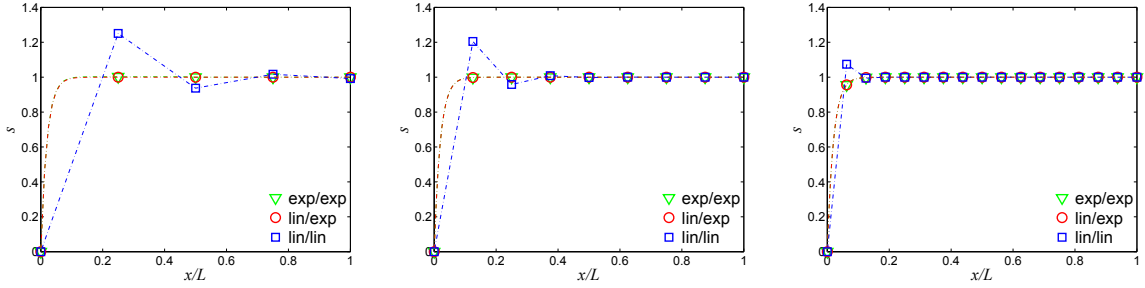
Figure 5: Solution of the 1d stationary evolution equation with $n = 4$ (left), $n = 8$ (middle) and $n = 16$ elements (right)
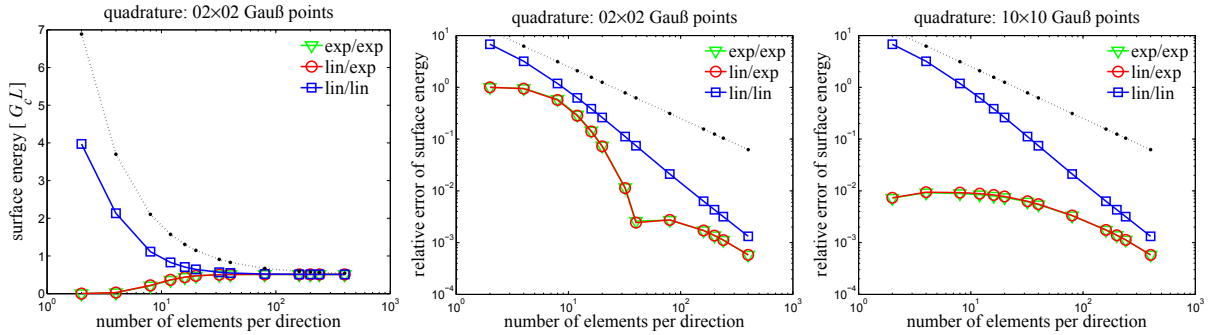

Figure 6: Evaluation of the surface energy

in Fig. 5. While there is almost no visible error in the solutions with exponential shape functions, the linear shape functions fail to adequately resolve the transition zone even for the smallest tested element size $h = L/16$.

5.2 Surface Energy of an Edge Notched Sample

For the first numerical assessment of the 2d exponential shape functions, the stationary evolution equation is solved on the domain $L \times L$ under the constraint $s(x, y) = 0$ if $(x, y) \in [0, L/2] \times \{0\}$. Again, the regularization length is set to $\epsilon = 0.01L$, and no mechanical loads are applied. A regular mesh with square elements is used for the discretization.

Figure 6 shows an evaluation of the surface energy E^{s} associated with the computed crack field. Regular meshes within the range of 2×2 to 400×400 elements were used for the discretization. The results are compared to the error estimate (18) for the triangular elements with linear shape functions (black dotted line). The reference solution $E^{\mathrm{s}} = 0.51017344300 \, \mathcal{G}_c L$ was computed with standard linear shape functions and a nonuniform mesh with square elements of edge length $h = 7.1429 \cdot 10^{-4} L$ in the vicinity the crack. The performance of the tested linear shape functions is slightly better than it is to be expected from the error estimate. However, especially for discretizations with only few
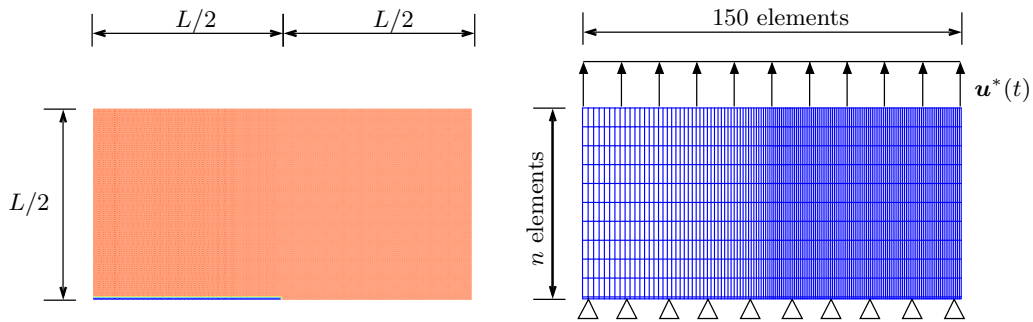
Figure 7: Simulation setup: contour plot of initial crack field (left) and finite element mesh (right)

elements both versions using the exponential shape functions perform significantly better. A crucial point for the performance of the exponential shape functions is a sufficiently precise computation of the integrals in the residuals (12), the stiffness matrix (14), and the damping matrix (15). For standard linear 4 node elements, usually the Gauß quadrature formula with 2 integration points per direction is used to compute the integrals. Yet, the performance of the exponential shape functions can easily be improved by employing a higher order quadrature method, e.g. a quadrature with 10×10 Gauß points as was used to obtain the results in the right plot of Fig. 6. Thus, a major part of the error in the surface energy computed with exponential shape functions and 2×2 Gauß points (Fig. 6, middle) is due to the quadrature error.

5.3 Peel Off Test

In this simulation the performance of the exponential shape functions is tested under mechanical loading, i.e. the whole set of coupled equations has to be solved..e. the whole set of coupled equations has to be solved. The mixed formulation (lin/exp) yields an unsymmetric system matrix, which is computationally more expensive. As the results obtained by the pure exponential formulation in sections 5.1 and 5.2 are very similar, the mixed formulation is dismissed in the following. The sample depicted in Fig. 7 is loaded by a linear increasing displacement load $\boldsymbol{u}^*(t) = \sqrt{\frac{\mathcal{G}_c L}{2\mu}} \cdot t$. A dimensional analysis shows that with this scaling of the displacements, the geometric length L and the cracking resistance $\mathcal{G}_c$ can be factored out of the equations. If additionally the mobility M is chosen large enough to assume quasi-static cracking, the solution of the coupled problem only depends on the ratio of the Lamé constants λ/μ (here: $\lambda = \mu$) and the regularization parameter ϵ in conjunction with L (here: $\epsilon = 0.0005L$). The discretization in x-direction is done with 150 elements. A varying number of n elements plus one row of elements of fixed height, to model the initial crack, discretize the structure in y-direction, see Fig. 7. Gauß quadrature with 5×5 integration points was used for the integration.

The two left plots in Fig. 8 show the evolution of the elastic energy with respect to the load factor t for different values of n. The elastic energy increases with the loading
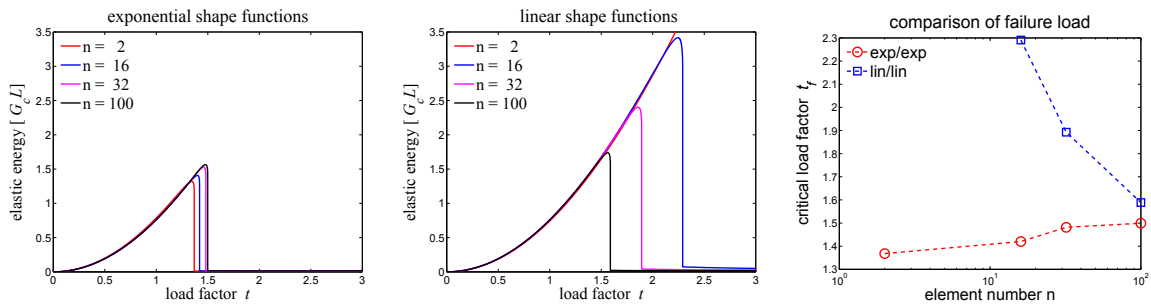
Figure 8: Elastic energy and failure load

until rupture occurs and it drops to zero. Impressively, the simulation with only $n = 2$ elements in y-direction already gives a qualitatively good result, when the exponential shape functions are employed. Using the standard linear shape functions, no rupture is observed in the simulation with $n = 2$ elements up to a load factor of $t = 3$, which is about twice the actual critical loading. Also the simulation with $n = 16$ elements still overestimates the critical loading by far. Only the simulations with more elements produce as accurate results as the simulations with the exponential shape functions. The right plot of Fig. 8 compares the computed failure loads. The overestimation of the critical load value of the linear shape functions stems from the overestimation of the surface energy associated with the initial crack.

6 SUMMARY

The aim of this work was to provide an alternative to expensive mesh refinement in finite element simulations of a phase field model for fracture in cases where the regularization parameter is very small. To this end special shape functions, which capture the analytical stationary solution of the 1d crack field, were derived and implemented into a 2d element of a finite element code. Through their dependence on the ratio of element size and regularization parameter, the exponential shape functions are able to adjust to the crack field for virtually arbitrarily small values of the regularization length. This allows for computations with very small values of the regularization parameter, which would require an extensive mesh refinement, when standard linear shape functions are used.

The effectiveness of the proposed technique has been demonstrated in numerical examples. In all simulations the usage of the exponential shape functions resulted in a considerable reduction of the level of refinement, yet their full potential only reveals itself if a sufficiently precise quadrature method is employed for the computation of the occurring integrals.

REFERENCES

[1] Francfort, G. A. and Marigo, J.-J. Revisiting brittle fracture as an energy minimization problem. *J. Mech. Phys. Solid.* (1998) **46**:1319–1342.

[2] Bourdin, B., Francfort, G. A. and Marigo, J.-J. Numerical experiments in revisited brittle fracture. *J. Mech. Phys. Solid.* (2000) **48**:797–826.

[3] Aranson, I. S., Kalatsky, V. A. and Vinokur, V. M. Continuum field description of crack propagation. *Phys. Rev. Let.* (2000) **85**:118–121.

[4] Karma A., Kessler, D. A. and Levine, H. Phase-field model of mode iii dynamic fracture. *Phys. Rev. Let.* (2001) **87**:45501.

[5] Eastgate, L. O., Sethna, J. P., Rauscher, M., Cretegny, T., Chen, C.-S. and Myers, C. R. Fracture in mode i using a conserved phase-field model. *Phys. Rev. E* (2002) **65**:036117.

[6] Brener, E. A. and Spatschek, R. Fast crack propagation by surface diffusion. *Phys. Rev. E* (2003) **67**:016112.

[7] Spatschek, R., Hartmann, M., Brener, E., Müller-Krumbhaar, H. and Kassner, K. Phase field modeling of fast crack propagation. *Phys. Rev. Let.* (2006) **96**:015502.

[8] Miehe, C., Welschinger, F. and Hofacker, M. Thermodynamically consistent phase-field models for fracture: Variational principles and multi-field fe implementations. *Int. J. Numer. Meth. Eng.* (2010) **83**:1273–1311.

[9] Welschinger, F., Hofacker, M. and Miehe, C. Configurational–force–based adaptive fe solver for a phase field model of fracture. In *PAMM* (2010) **10**:689–692.

[10] LaZghab, S., Aukrust, T. and Holthe, K. Adaptive exponential finite elements for the shear boundary layer in the bearing channel during extrusion. *Comput. Meth. Appl. Mech. Eng.* (2002) **191**:1113–1128.

[11] Bourdin, B. Numerical implementation of the variational formulation of quasi-static brittle fracture. *Interfaces Free Bound.* (2007) **9**.

[12] Bourdin, B., Francfort, G. and Marigo, J.-J. The variational approach to fracture. *J. Elasticity* (2008) **91**:5–148.

[13] Amor, H., Marigo, J.-J. and Maurini, C. Regularized formulation of the variational brittle fracture with unilateral contact: Numerical experiments. *J. Mech. Phys. Solid.* (2009) **57**:1209–1229.

[14] Kuhn, C. and Müller, R. A new finite element technique for a phase field model of brittle fracture. *J. Theor. Appl. Mech* (2011) in press.